

REMARKS

Claims 26-50 are pending in the present application. Claims 34, 36, and 37 have been amended and claims 42-50 have been withdrawn without prejudice to or disclaimer of the subject matter contained therein. Support for the amendments may be found throughout the application as filed, for example, on page 4, lines 22-28 and page 8, lines 9-14. No new matter is added by way of amendment.

Reexamination of the application and reconsideration of the rejections and objections are respectfully requested in view of the above amendments and the following remarks, which follow the order set forth in the Office Action.

Rejections under 35 U.S.C. § 102

Claims 26, 29-31 and 41 were rejected under 35 U.S.C. § 102(e) as being anticipated by U.S. Patent No. 6,790,556 to Meitav et al. ("Meitav"). Applicants respectfully traverse.

Applicants respectfully submit that Meitav does not disclose an energy storage device in which the elements are coated in part at least by a protective layer formed of a metal or metal alloy having an expansion coefficient less than $6 \times 10^{-6} \text{ }^{\circ}\text{C}^{-1}$, as required by claim 26. Meitav discloses electrochemical systems for storage and release of electrical energy, which may have an outer case made of stainless steel. See, c. 1, ll. 10-20; c. 7, ll. 12-25; and Figs. 3A-B. Meitav discloses that the outer surface of the stainless steel case may also be coated with a highly conductive material, such as gold, nickel, platinum, silver, lead, tin, or brass. See, c. 7, ll. 19-24. Stainless steel has an expansion coefficient of $18 \times 10^{-6} \text{ }^{\circ}\text{C}^{-1}$, as reported by Haddar, N. et al., "Thermal fatigue crack networks: a computational study" International Journal of Solids and Structures 42: 771-778 (2005), ("Haddar", attached as Exhibit A). See, p. 773, ¶2 and p. 775, ¶4.¹ Further, the expansion coefficients of the additional metals disclosed in Meitav as potential coatings are greater than $6 \times 10^{-6} \text{ }^{\circ}\text{C}^{-1}$ (i.e., gold, nickel, platinum, silver, lead, tin, and brass). See, "The Engineering Toolbox: Coefficients of Linear Expansion", attached as Exhibit B.²

¹ Haddar studied AISI 304L type stainless steel. See, p. 773, ¶2. Haddar stated that the data for AISI 304L adopted for calculations included an average coefficient of thermal expansion of $18 \times 10^{-6} \text{ }^{\circ}\text{C}^{-1}$. See, p. 775, ¶4.

² The linear expansion coefficient (10^{-6} K^{-1}) of gold is 14.2, nickel is 13.0, platinum is 9.0, silver is 19.5, lead is 28.0, tin is 23.4, and brass is 18.7. This reference is available at www.engineeringtoolbox.com.

Since the Office has not shown that all of the claim limitations are disclosed by Meitav, Applicants respectfully submit that the instant claims are not anticipated by Meitav and thus respectfully request withdrawal of the rejection.

Rejections under 35 U.S.C. § 103

I. Meitav and Sekido

Claim 27 was rejected under 35 U.S.C. § 103(a) as being unpatentable over Meitav in view of U.S. Patent No. 4,148,976 to Sekido et al. ("Sekido"). Applicants respectfully traverse.

Meitav and Sekido, alone or in combination, do not teach or suggest a protective layer formed of a metal or metal alloy having an expansion coefficient less than $6 \times 10^{-6} \text{ }^{\circ}\text{C}^{-1}$, as required by claim 27. As discussed above, Meitav does not disclose a protective layer formed of a metal or metal alloy having an expansion coefficient less than $6 \times 10^{-6} \text{ }^{\circ}\text{C}^{-1}$. Sekido teaches a current collector metal made of ferrite stainless steel containing at least 30 wt. % of Cr and at least 2 wt % of Mo. See, c. 2, ll. 59-64; c. 4, ll. 34-37; c. 5, ll. 4-16; and Table 1. The stainless steel alloys disclosed in Sekido that contain molybdenum also contain chromium. Id.

Sekido does not remedy the deficiency of Meitav because it does not teach or suggest that the super ferrite stainless steel containing at least 30 wt. % of Cr and at least 2 wt % of Mo disclosed therein has an expansion coefficient less than $6 \times 10^{-6} \text{ }^{\circ}\text{C}^{-1}$, particularly in view of the expansion coefficient of $18 \times 10^{-6} \text{ }^{\circ}\text{C}^{-1}$ for stainless steel. Thus, a combination of the teachings of Meitav and Sekido would not lead to a protective layer formed of a metal or metal alloy having an expansion coefficient less than $6 \times 10^{-6} \text{ }^{\circ}\text{C}^{-1}$, as required by claim 27.

Since the Office has not shown that all of the claim limitations are taught or suggested by Meitav and Sekido, Applicants respectfully submit that the instant claims are not obvious over the combination of Meitav and Sekido and thus respectfully request withdrawal of the rejection.

II. Meitav and Neudecker

Claims 32-33 and 37-38 were rejected under 35 U.S.C. § 103(a) as being unpatentable over Meitav in view of U.S. patent No. 6,168,884 to Neudecker et al. ("Neudecker"). Applicants respectfully traverse.

Applicants respectfully submit that claims 32-33 and 37-38 are patentable over Meitav and Neudecker because the Office has not shown that Neudecker teaches or suggests a protective layer formed of a metal or metal alloy having an expansion coefficient less than $6 \times 10^{-6} \text{ }^{\circ}\text{C}^{-1}$, as required by claims 32-33 and 37-38.

The teachings of Meitav were discussed more fully above. Neudecker teaches a lithium battery precursor with an anode current collector sandwiched between a solid state electrolyte and an overlying layer. See, c. 1, ll. 43-52 and c. 4, ll. 28-29. Neudecker also teaches a cathode that is covered by a cathode film made of a transition metal oxide such as LiCoO_2 or LiMn_2O_4 . See, c. 3, ll. 57-59. Neudecker further teaches that the overlying layer over the anode can be made of lithium phosphorous oxynitride or aluminum nitride. See, c. 4, ll. 28-38.

There is no teaching or suggestion within Neudecker that transition metal oxides, such as LiCoO_2 or LiMn_2O_4 , lithium phosphorous oxynitride or aluminum nitride have an expansion coefficient less than $6 \times 10^{-6} \text{ }^{\circ}\text{C}^{-1}$. Further, the Office has not provided any evidence that these materials have an expansion coefficient less than $6 \times 10^{-6} \text{ }^{\circ}\text{C}^{-1}$. Accordingly, the Office has not shown that Meitav or Neudecker, alone or in combination, teaches or suggests a protective layer formed of a metal or metal alloy having an expansion coefficient less than $6 \times 10^{-6} \text{ }^{\circ}\text{C}^{-1}$, as required by claims 32-33 and 37-38.

Since the Office has not shown that all of the claim limitations are taught or suggested by Meitav and Neudecker, Applicants respectfully submit that the instant claims are not obvious over the combination of these references and thus respectfully request withdrawal of the rejection.

III. Meitav, Neudecker and Katz

Claim 36 was rejected under 35 U.S.C. § 103(a) as being unpatentable over Meitav in view of Neudecker and further in view of U.S. Patent No. 6,200,704 to Katz et al. ("Katz"). Applicants respectfully traverse.

The teachings of Meitav and Neudecker are discussed more fully above. Katz discloses a battery and a positive electrode having an "active-sulfur" material and a second electrochemically active material having a higher discharge rate than the active-sulfur component. See, Abstract; c. 2, ll. 51-61; and c. 3, ll. 28-37. The positive electrode may include protective layer forming additives to protect a lithium negative electrode, which include organosulfur compounds, phosphates, iodides, iodine, metal sulfides, nitrides, and

fluorides. See, c. 9, ll. 18-21. The negative electrode can also have a protective layer on the electrolyte side. See, c. 14, ll. 62-63. The Office has not provided any evidence showing that any of these materials in Katz has an expansion coefficient less than $6 \times 10^{-6} \text{ }^{\circ}\text{C}^{-1}$, as required by claim 36.

Since the Office has not shown that all of the claim limitations are taught or suggested by Meitav, Neudecker and Katz, Applicants respectfully submit that the instant claims are not obvious over the combination of these references and thus respectfully request withdrawal of the rejection.

IV. Meitav, Neudecker and Verma

Claims 39-40 were rejected under 35 U.S.C. § 103(a) as being unpatentable over Meitav in view of Neudecker, and further in view of U.S. Patent Publication No. 2002/0071989 to Verma et al. ("Verma"). Applicants respectfully traverse.

The teachings of Meitav and Neudecker are discussed more fully above. Verma teaches a thin-film battery with a protective coating including thin films of any two dielectric materials, such as aluminum oxide, silicon dioxide, silicon nitride, silicon carbide, tantalum oxide, diamond and diamond-like carbon. See, ¶[0026]. The Office has not provided any evidence showing that any of these materials has an expansion coefficient less than $6 \times 10^{-6} \text{ }^{\circ}\text{C}^{-1}$, as required by claims 39-40.

Since the Office has not shown that all of the claim limitations are taught or suggested by Meitav, Neudecker and Verma, Applicants respectfully submit that the instant claims are not obvious over the combination of these references and thus respectfully request withdrawal of the rejection.

Allowable Subject Matter

Applicants note that the Examiner stated that claim 28 would be allowable if rewritten in independent form.

For the foregoing reasons, claims 26-50 are considered allowable. A Notice to this effect is respectfully requested. If any questions remain, the Examiner is invited to contact the undersigned at the number given below.

The Director is hereby authorized to charge any appropriate fees that may be required by this paper, and to credit any overpayment, to Deposit Account No. 23-1925.

Respectfully submitted,

BRINKS HOFER GILSON & LIONE

Date: 10 / 11 / 2010

By: Daniel A. Rubé

Daniel A. Rubé
Registration No. 53,536

P.O. Box 110285
Research Triangle Park, NC 27709
Phone: 919.481.1111

Attachments: Exhibits A and B

Exhibit A



Thermal fatigue crack networks: an computational study

N. Haddar ^{a,*}, A. Fissolo ^a, V. Maillot ^b

^a CEA-DEN-SEMT-LISN Commissariat à l'Energie Atomique—Saclay, 91191 Gif sur Yvette Cedex, France

^b CEA-DEN-SRMA-LC2M Commissariat à l'Energie Atomique—Saclay, 91191 Gif sur Yvette Cedex, France

Received 1 June 2004; received in revised form 8 June 2004

Available online 18 September 2004

Abstract

Various components of nuclear reactors experience various thermo-mechanical loading. Thermal fatigue cracking has been clearly detected in reactor heat removal system (RHRS) of Pressurized Water Reactors (PWRs). The study presented here is focused on the AISI 304L stainless steel used in PWRs. The thermal fatigue behavior of this steel has been investigated using a specific thermal fatigue facility called “SPLASH test”. This test equipment allows the reproduction of multiple cracking networks similar to those detected during inspections. The present study deals with the modeling of cracking network development. It is structured in two parts: (i) experimental results and main characteristics of the crack networks, and (ii) numerical simulation on the multiple crack growth problem, using a modified stress intensity factor, and a generalized Paris' law. In spite of simplified assumptions, the model predictions are in good agreement with observations, as far as the evolution of the mean and deepest cracks during cycling are concerned. © 2004 Elsevier Ltd. All rights reserved.

Keywords: Thermal loading; Crack network; Crack propagation; Shielding effect

1. Introduction

Thermal fatigue induces in-service damage in various industrial components, such as moulds, rolling mill cylinders or turbine blades. Some examples are given by Bressers and Rémy (1996), Spera and Mowbray (1976) or Fissolo et al. (1996). Such damage sometimes also occurs in different types of nuclear reactor components. In the case of Pressurized Water Reactors (PWRs), crack networks may appear in auxiliary loop zones, close to a cold water injection site, in spite of relatively small temperature fluctuations (Keroulas and Thomeret, 1990). In May 1998, a leak occurred in the reactor heat removal system (RHRS) of the Civeaux1

* Corresponding author. Tel.: +33 169 089 101; fax: +33 169 088 784.

E-mail address: jbr1@semt2.smts.cea.fr (N. Haddar).

plant. The major root cause of cracking was identified as high cycle thermal fatigue (Cipière and Le Duff, 2001). Experiment tests were carried out for developing crack network under thermal fatigue loading using specific specimen and equipment. The present study is focused on the crack networks obtained with the SPLASH facility as described in the first part of this paper. In most cases, the crack propagation depth is small. The propagation and the shielding effect of the cracks in the network are therefore investigated numerically under thermal fatigue using a crack propagation simulation, as reported in the second part of this work.

2. Experimental set-up

2.1. The SPLASH equipment

For in-service components, thermo-mechanical loadings usually come from temperature gradients across the wall thickness. The SPLASH equipment was developed in order to reproduce such gradients on two opposite sides of a parallelepiped specimen.

Fig. 1 presents the specimen geometry. It is continuously heated by an electrical DC current (Joule effect), and cyclically submitted to thermal shocks (corresponding to a cooling rate of about 500–1000 °C/s) when water is sprayed on opposing faces.

Two types of specimens are used: calibration specimens and test specimens. Both are instrumented with four K-type thermocouples brazed in depth, at 3 and 7 mm from the left and right surfaces. Calibration specimens carry two additional thermocouples brazed at the center of the left and right quenched surfaces

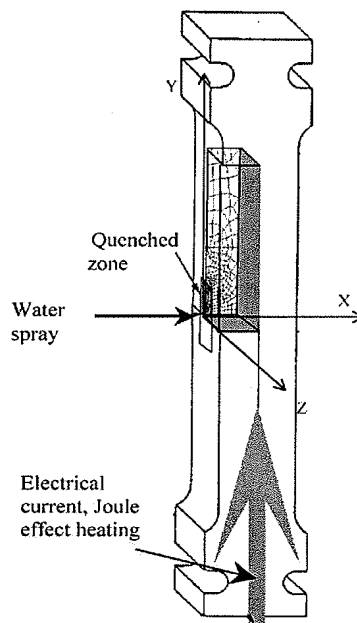


Fig. 1. SPLASH specimen.

Table 1
Thermal test conditions

T_{\max} (°C)	ΔT (°C)	Number of cycles to initiation	Total number of cycles	Number of specimens
320	125	190,000	500,000	1
320	150	70,000–80,000	300,000–700,000	4
320	200	50,000–60,000	150,000–300,000	2

and are used to determine the parameters of the water spray and the electrical current necessary to obtain the selected thermal loading. The test specimens are not equipped with those surface thermocouples, in order to avoid premature crack initiation.

The steel studied here is a AISI 304L type austenitic stainless steel.

The thermal conditions studied are given in Table 1.

The number of cycles to initiation N_i is determined by optical microscopy observations at regular time intervals of the quenched surfaces, after the removal of the thin oxide layer that forms during cycling. It is considered that initiation occurs when at least one of 50–150 μm long crack is observed (Fissolo et al., 2000). The formation of a network is observed regularly during the test. Then the test is stopped at a chosen number of cycles. After the end of the test, the 3D characterization of the crack networks is performed, using a step-by-step removal of thin layers (Maillot et al., 2004).

2.2. Network parameters

In order to characterize the growth of the networks, various geometrical and statistical parameters are determined on the surface of the specimen during the cycling, and in depth, at the end of the test (Maillot, 2004).

2.2.1. Evolution of the network on surface

It takes time for the first cracks to grow, coalesce and form a network on the surface of the specimen. The crack density is used to quantify the stability of a crack network. It is calculated for a chosen reference surface which should correspond roughly to the uniform temperature region obtained on the SPLASH specimen during the thermal shock. The density is obtained by dividing the total length of all cracks by the area of this reference surface. For tests performed with $\Delta T = 150$ °C for example, such a surface is defined as 200,000 cycles. Although the scatter of the data may be large, we can consider that a stabilization of the crack network is obtained on the surface after 400,000 cycles as shown in Fig. 2.

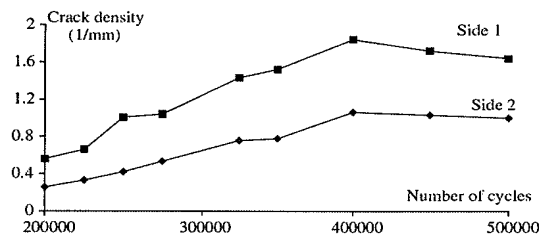


Fig. 2. Crack density versus the number of cycles ($T_{\max} = 320$ °C, $\Delta T = 150$ °C).

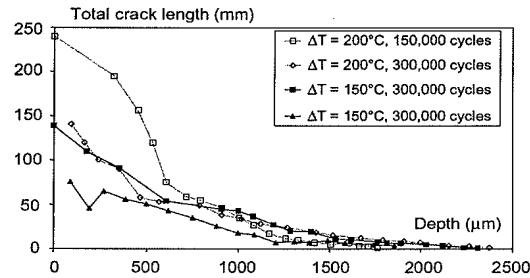


Fig. 3. Total crack length versus the depth ($T_{\max} = 320\text{ }^{\circ}\text{C}$).

2.2.2. Evolution of the network in depth

Because of the loading itself, there is a strong loading gradient in the specimen depth. Therefore, the cracks cannot propagate very deep into the material. Furthermore, there is also a shielding effect, between neighboring cracks, that slows down and then stops the propagation of the smaller ones.

Those effects appear clearly in Fig. 3. The total crack length quickly becomes smaller after a few hundred micrometers, as most cracks stop. The complexity of the network also decreases as the depth increases, because only a few of the most important cracks still propagate. The figure shows that longer cracks do not exceed 2.4 mm length even for the most severe loading ($\Delta T = 200\text{ }^{\circ}\text{C}$) after 300,000 cycles. Experimental observations in depth show that only one or two cracks reach the maximum depth (Maillot, 2004). In any case, such dominant cracks propagate in the middle of the quenched zone.

3. Simulation

Here, we discuss simulation of the propagation of a thermal cracking network in two dimensions. We first present the thermal-mechanical calculation on a quarter of a specimen without cracks. Such a calculation will give us the mechanical quantities induced by the imposed thermal shock. In the second step, we develop a procedure for the calculation of the propagation of a parallel crack network. This procedure will be based on the thermo-mechanical calculation made later on, by assuming that the coupling cracks—mechanical field is less important than the shielding effect.

3.1. Thermal-mechanical simulation

The objective of this simulation is to determine the strain and stress fields within the specimen, during cycling.

Calculations are carried out with the finite element code of CEA, CAST3M. Taking advantage of symmetries a quarter of the relevant part of the SPLASH specimen is modeled in two dimensions.

The calculations are carried out twice:

- initially, purely thermal analysis. By adjusting the heat flux into the specimen, we try to match the evolution of the temperature measured during a stabilized cycle at the various positions of the thermocouples on a calibration specimen,

- subsequently, the resulting time-dependent temperature fields entail a certain stress and strain, where the material behavior is described by an elastic–plastic law with isotropic as well as kinematic hardening (Chaboche, 1989). Elastic–plastic law is identified with low cycle fatigue tests performed at the maximum temperature $T = 320\text{ }^{\circ}\text{C}$.

3.1.1. Evolution of temperatures

The FE-mesh used is presented in Fig. 5. A very fine mesh is used in the critical zone, i.e. the one located immediately under the quenched zone. The thermal boundary conditions are chosen as follows (Fig. 4):

- adiabatic conditions along the lines of symmetry,
- a heat source being constant over time, corresponding to the Joule effect loading to a uniformly distributed heating of the specimen,
- a heat flux leaving the front face of the specimen, in the zone not exposed to the water spray, corresponding to the convection of air on the free face of the specimen,
- a heat flux leaving the quenched zone of the front face of the specimen, variable in time, corresponding to the convection by water at the time of quenching and to the convection of the air during the remainder of the cycle, called flow of quenching.

To define the heat flux away from the quenched zone as a function of time, the thermal cycle is divided into four phases, as presented in Fig. 6. The application of the quenching flux should be nearly instantaneous on the zone of thermal variations. However, an instantaneous jump of the flux from air convection to forced convection due to water spray quenching causes numerical oscillations of the temperature calculated on the surface. Such oscillations have not any physical meaning. To eliminate this problem, we chose to a time of 0.02 s (to be compared with the duration of the quenching of 0.25 s) for the transition from free to forced convection (Fig. 6).

The material is supposed to have an isotropic thermal behavior. The data of the AISI 304L adopted for the calculations are as follows: ρ , volume mass: 7800 kg/m^3 ; C , specific heat: $500\text{ J kg}^{-1}\text{ K}^{-1}$; K , thermal conductivity: $19\text{ W m}^{-1}\text{ K}^{-1}$; α , average coefficient of thermal expansion: $18 \times 10^{-6}/^{\circ}\text{C}$.

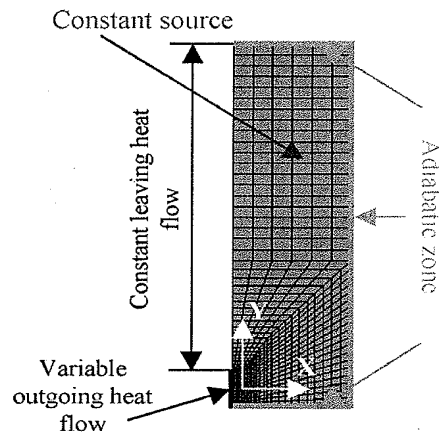


Fig. 4. Thermal boundary conditions of the model.

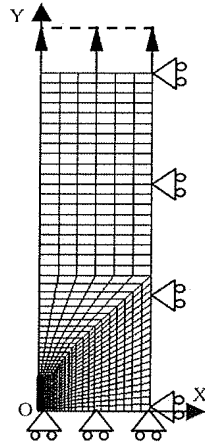


Fig. 5. Finite element mesh: mechanical boundary conditions.

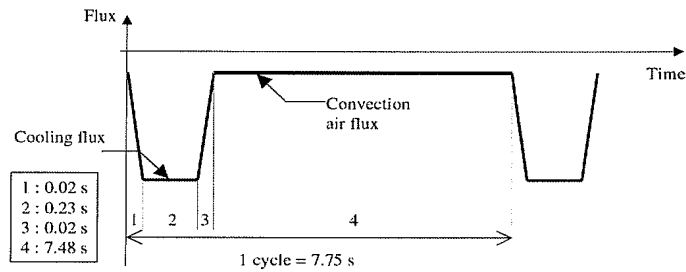


Fig. 6. Evolution of thermal conditions in the quenched zone.

The values of the various flux are adjusted until the evolution of the temperatures obtained on the corresponding thermocouple positions agree best with the experimentally measured temperatures (Fig. 7).

3.1.2. Stress and strain fields

The temperature fields determined previously in a thermal analysis are applied to a 2D model for the mechanical calculations with symmetric displacement boundary conditions (Fig. 5). The evolution of the stress field as function of time can be given at any point of the specimen: the temperatures are imposed on the nodes under plane strain conditions. The result of the calculations give e.g. the distribution of the stress component σ_{yy} along the axis ox (depth direction) which is presented in Fig. 8, depicted for $t = 0.25$ s (almost at the end of the cooling down to T_{\min}), and for $t = 7.75$ s (end of the increase in temperature up to T_{\max}); the third curve represents the variation of stress σ_{yy} during a thermal cycle.

One of the assumptions that we formulated previously, was the equibiaxiality of mechanical quantities on the surface. Fig. 9 compares the evolution of the various variations of principal stress according to the depth during a cycle. It shows that this equibiaxiality on the surface is about satisfied for $T_{\max} = 320$ °C, and $\Delta T = 200$ °C.

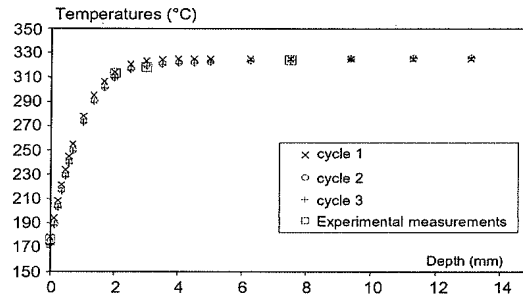


Fig. 7. Evolution of the minimum temperatures versus the depth for three cycles: comparison with experimental measurements $T_{\max} = 320$ °C, $\Delta T = 150$ °C.

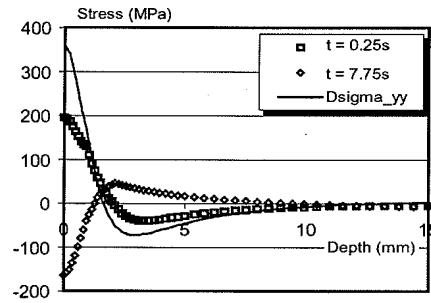


Fig. 8. Evolution of the σ_{yy} stress at T_{\min} and T_{\max} and the stress range $\Delta\sigma_{yy}$ during one cycle, as function of the depth ($T_{\max} = 320$ °C, $\Delta T = 200$ °C).

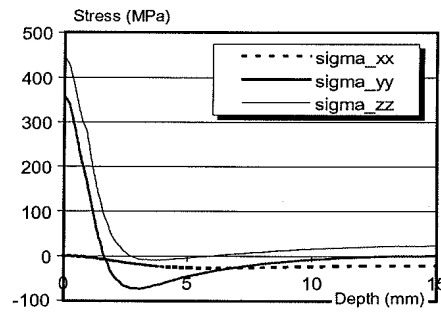


Fig. 9. Evolutions of the principal stress variations $\Delta\sigma_{xx}$, $\Delta\sigma_{yy}$ and $\Delta\sigma_{zz}$ as function of the depth ($T_{\max} = 320$ °C, $\Delta T = 200$ °C).

The maximum variation of the stress obtained on the surface by means of the finite element method, are 359 MPa for $\Delta\sigma_{yy}$ and 446 MPa for $\Delta\sigma_{zz}$. The stress range $\Delta\sigma_{yy}$, likely to open crack bands parallel to an xz -plane is equal to 359 MPa on the surface; it decreases in-depth and vanishes at about 1.6 mm of depth,

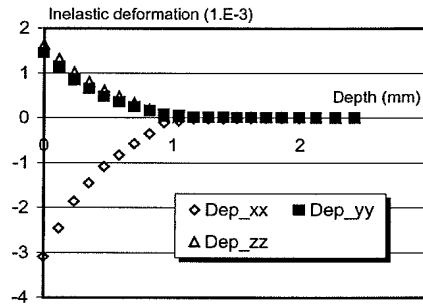


Fig. 10. Evolution of the inelastic strain range $\Delta\epsilon_{p_{xx}}$, $\Delta\epsilon_{p_{yy}}$ and $\Delta\epsilon_{p_{zz}}$ as function of depth ($T_{\max} = 320^\circ\text{C}$, $\Delta T = 200^\circ\text{C}$).

becomes negative beyond that point. The 1.6 mm depth then calculated gives the order of magnitude beyond which a crack is no longer subjected to an opening stress.

The SPLASH loading generates plastic strain which extend up to 1 mm depth in the middle from the quenched zone, as shown in Fig. 10. For cracks the plastic behavior of the material has to be taken into account since it obviously has an effect on the crack propagation.

On the surface, we notice that the plastic strain range varies according to the distance from the middle of the quenched zone (Fig. 11). Although the imposed heat flux is constant, the boundary conditions make sure that the inelastic strain decreases towards the periphery of the quenching window. Thus, according to the position of the crack on the specimen and its length, the response will be different. Taking into account this distribution seems important to us in the calculation of the propagation of the crack network.

3.1.3. Influence of thermal conditions on mechanical loading

The elastic–plastic calculations are carried out for three thermal conditions (for the same maximum temperature 320°C). Fig. 12 gives the variation of the stress σ_{yy} during a cycle versus the depth for three temperature ranges. The general shape of the curves is comparable for all conditions. The stress level in the surface is influenced by the thermal condition. This difference disappears in the depth of the specimen. Fig. 13 represents the variation of σ_{yy} on the surface for different temperature ranges. As for the inelastic strain, we notice that $\Delta\sigma_{yy}$ varies on the surface. The level of stress is constant in the middle of the quenched

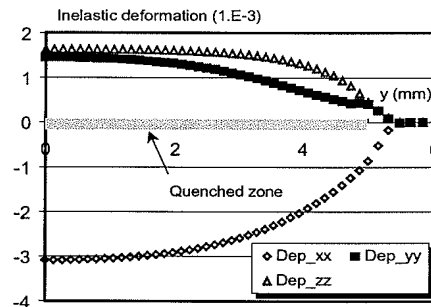


Fig. 11. Evolution of the inelastic strain range $\Delta\epsilon_{p_{xx}}$, $\Delta\epsilon_{p_{yy}}$ and $\Delta\epsilon_{p_{zz}}$ in surface ($T_{\max} = 320^\circ\text{C}$, $\Delta T = 200^\circ\text{C}$).

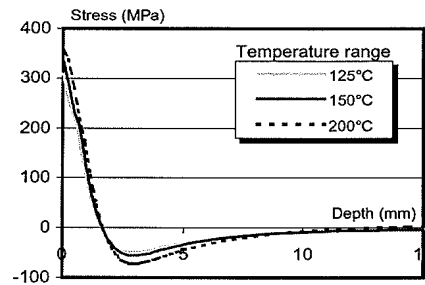


Fig. 12. Evolution of the variation of stress $\Delta\sigma_{yy}$ in depth for three temperature ranges.

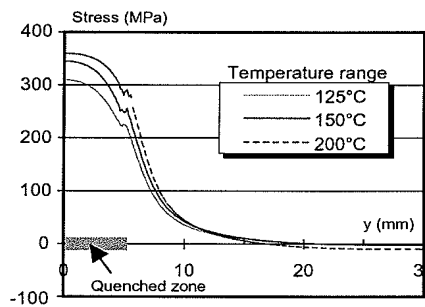


Fig. 13. Evolution of the variation of stress $\Delta\sigma_{yy}$ on the surface for three temperature ranges.

zone, the more we move away the more it decreases. For the three conditions the level of stress is nearly cancelled at a distance of 20 mm from the middle of the quenched zone.

3.2. Crack propagation model

The 2D model was designed to take into account for the in-depth propagation of multiple cracks under thermal loading conditions. The model which is to develop thereafter is composed of two stages as shown in Diagram 1:

- The first stage simulates the initiation of the thermal fatigue network. As a first assumption, we will suppose that the network is already existing at the beginning. The sizes of the cracks correspond to those of the grain diameters and their spacing corresponds to the experimental spacing which was observed in the middle of the network.
- The second stage deals with the propagation of this network. The propagation program is divided into three steps:
 - In the first step, half a specimen is meshed including a crack network.
 - In the second step, an equivalent elastic load deduced from the stress field calculated later is applied. Here a modified stress intensity factor comes into play. By supposing that the interaction between cracks plays a more important part than the effect of the cracks on the loading, the calculated stresses will be applied directly to the flanks of each crack.

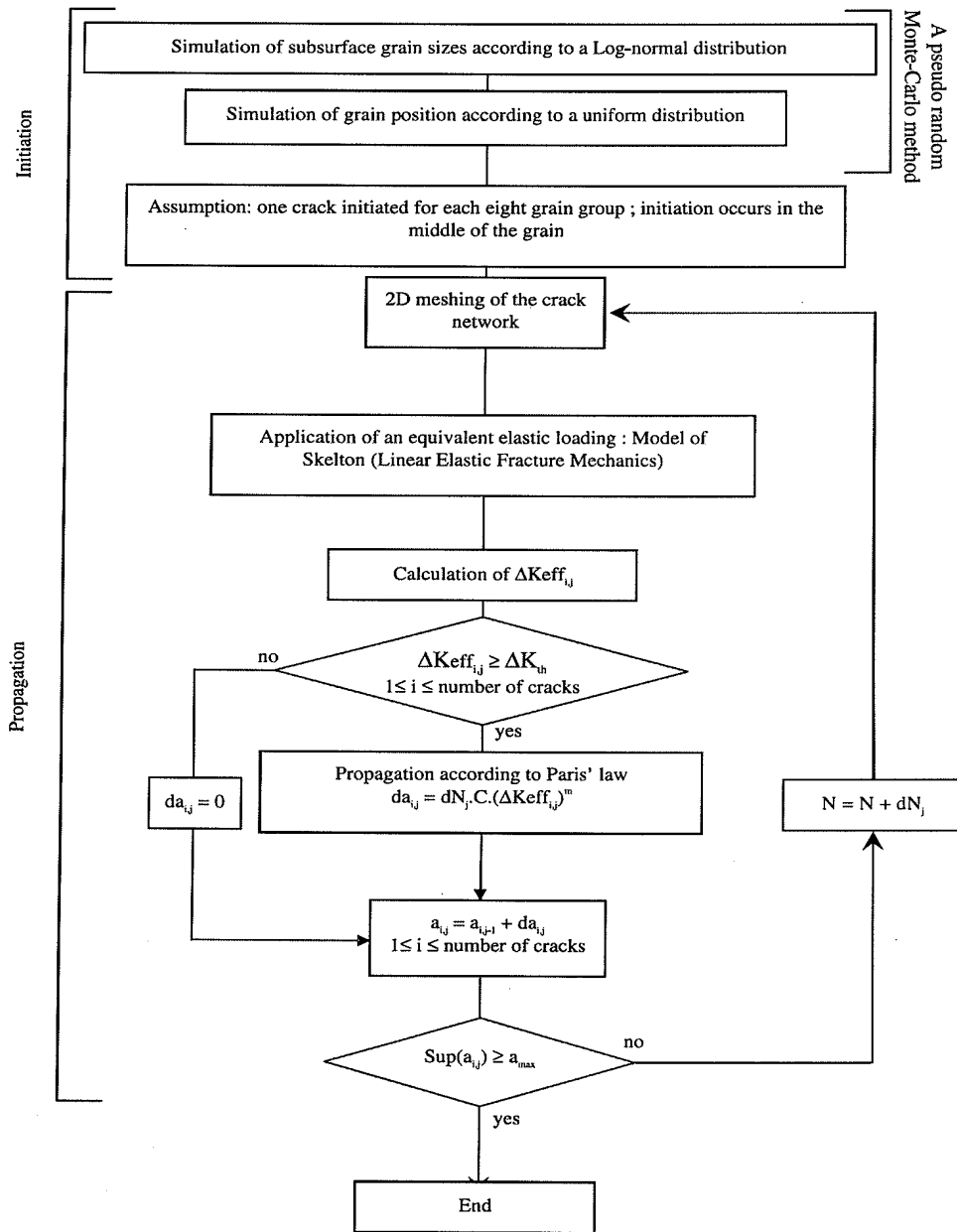


Diagram 1. Propagation of a crack network due to thermal fatigue.

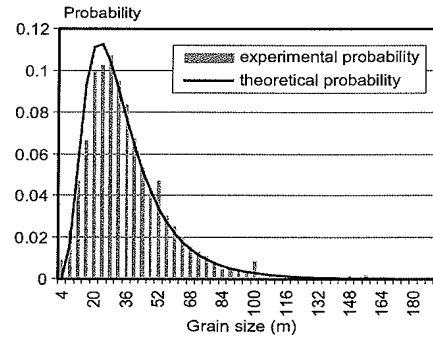


Fig. 14. Experimental and theoretical distribution of the sizes of austenite grain: distribution assimilable to a log-normal law.

- In the third step, the incremental growth of each crack is determined by calculating the variation of its stress intensity factor (ΔK_{eff}) and by applying Paris' law.

Several iterations will be carried out until reaching a given size of a maximum allowable crack (Diagram 1).

3.2.1. Initiation

The simulation of crack initiation is performed in two steps. In the first step, a Monte Carlo randomization method (Binder and Heermann, 2002) is used to determine the size of the surface grains, according to a distribution law of the experimentally measured grain sizes (Fig. 14). The obtained grains are square-shaped. In the second step, another Monte Carlo randomization assigns each grain a position relative to the surface.

In the present state of the model, it is assumed that right from the beginning, one out of eight grains is completely cracked through the middle. This assumption is not unreasonable as can be concluded from the experimental spacing of the cracks in the formed network. However, it is still an oversimplification since it was observed experimentally that the cracks do not appear at the same time. Nevertheless this initiation hypothesis is employed so that, the simulation of the crack propagation can be performed.

3.2.2. Propagation

First the thermo-mechanical loading has to be calculated. Near the surface, the stresses are equibiaxial. Skelton's model (Skelton, 1983) is used to define an equivalent stress intensity factor Eq. (1). According to Eq. (2), the strain loading can be reduced to an elastic stress loading which follows the laws of Linear Elastic Fracture Mechanics:

$$\Delta\sigma_{\text{eff}} = q \cdot \Delta\sigma + \Delta\sigma_{\text{pseudo}} \quad (1)$$

$$\Delta\sigma_{\text{pseudo}} = \frac{E}{(1-2\nu)(1+\nu)} [(1-\nu)\Delta\epsilon_{yy} + \nu\Delta\epsilon_{xx} + \nu\Delta\epsilon_{zz}] \quad (2)$$

$q \cdot \Delta\sigma$ represents the part of the cycle when the crack is open, while it takes into account the plasticity at the crack tip. For the present purpose, q was estimated to be close to 0.9.

$\Delta\sigma_{\text{eff}}$ is fitted with two polynomials as function of depth (x) and surface distance from the middle of the thermal shock (y) as presented in Eq. (3):

$$\begin{aligned}\Delta\sigma_{\text{eff}} &= f(x) \cdot g(y) \\ f(x) &= A_0 + A_1x + A_2x^2 + A_3x^3 + A_4x^4 + A_5x^5 \\ g(y) &= B_0 + B_1y + B_2y^2 + B_3y^3 + B_4y^4 + B_5y^5 + B_6y^6\end{aligned}\quad (3)$$

The parameters A_i and B_j are given in the following tables for different thermal conditions.

ΔT (°C)	A_0	A_1	A_2	A_3	A_4	A_5
125	371.16	-412.16	150.08	-25.18	2.003	-0.0612
150	437.3	-475.89	170.44	-28.15	2.206	-0.0664
200	537.25	-569.59	197.08	-31.34	2.362	-0.0683

ΔT (°C)	B_0	B_1	B_2	B_3	B_4	B_5	B_6
125, 150 and 200	0.9995	0.0072	-0.0309	0.0194	-0.0082	0.0013	-7.02E-5

For the three studied temperature ranges, Fig. 15 represents the evolution of the effective stress versus the depth of the specimen. For $\Delta T = 200$ °C, for example, $\Delta\sigma_{\text{eff}}$ decreases from 500 MPa on the surface to -50 MPa at 2.5 mm depth. The same shape of the curve is obtained for the other two levels of loading ($\Delta T = 150$ °C and $\Delta T = 125$ °C). The range of the effective stress decreases when the range temperature decreases.

The distribution of the effective stress on the surface (Fig. 16), shows that up to 1 mm of the middle of the quenched zone, the effective stress range remains constant. The more we move away from the middle of the specimen the more the level of stress decreases. At the edges of the quenched zone for example, only 60% of the maximum stress (in the middle of the quenched zone) are reached.

ΔK_{eff} is then calculated using the superposition method of Buchalet and Bamford (1976), as presented in Eq. (4a), for a crack of depth a and position y in the quenched line:

$$\Delta K_{\text{eff}}(a, y) = \sqrt{\pi a} \cdot g(y) \cdot \left[A_0 F_1 + \frac{2a}{\pi} A_1 F_2 + \frac{a^2}{2} A_2 F_3 + \frac{4a^3}{3\pi} A_3 F_4 + \frac{a^4}{4} A_4 F_5 + \frac{6a^5}{5\pi} A_5 F_6 \right] \quad (4a)$$

where F_1, F_2, F_3, F_4, F_5 and F_6 depend on the geometry, and particularly on the other cracks (depths and distances from the studied crack) Eq. (4b).

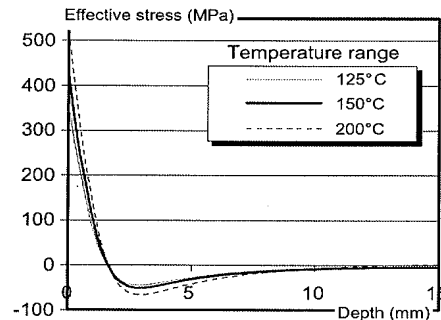


Fig. 15. Evolution of the effective stress versus the depth.

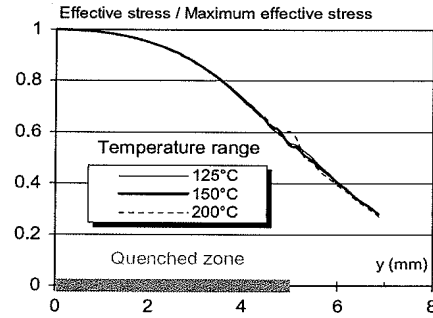


Fig. 16. Distribution of the effective stress range on the surface.

$$\begin{aligned}
 F_1 &= \frac{\Delta K(\sigma = A_0)}{A_0 \sqrt{\pi a}}; & F_2 &= \frac{\sqrt{\pi}}{2A_1 \sqrt{a^3}} \Delta K(\sigma = A_1 x) \\
 F_3 &= \frac{2}{\sqrt{\pi} A_2 \sqrt{a^5}} \Delta K(\sigma = A_2 x^2); & F_4 &= \frac{3\sqrt{\pi}}{4A_3 \sqrt{a^7}} \Delta K(\sigma = A_3 x^3) \\
 F_5 &= \frac{4}{\sqrt{\pi} A_4 \sqrt{a^9}} \Delta K(\sigma = A_4 x^4) & \text{and} & F_6 = \frac{5\sqrt{\pi}}{6A_5 \sqrt{a^{11}}} \Delta K(\sigma = A_5 x^5)
 \end{aligned} \tag{4b}$$

The growth of each crack then follows a generalized Paris' law, as presented in Eq. (5), for a given increment of cycles.

$$da_i = C.(\Delta K_{\text{eff},i})^m dN \tag{5}$$

where

$$C = 2.05 \times 10^{-10} \frac{\text{mm}}{\text{cycle}} (\text{MPa}\sqrt{\text{m}})^{-m}; \quad m = 4.2$$

3.3. Results and discussion

3.3.1. Single crack propagation

Initially, we studied the propagation of a single crack under SPLASH thermal loading. The crack is located at the middle of the surface specimen. By applying the procedure of propagation (described previously) starting from an initial size of 0.12 mm, we obtain the evolution of the stress intensity factor ΔK_{eff} according to the crack size (Fig. 17). Under SPLASH loading, we notice that the stress intensity factor increases when the size of the crack increases up to a size of 0.7 mm. For higher depth, we primarily notice a decrease of the S.I.F due to the decrease of the resulting mechanical loading.

By applying a standard Paris' law, we obtain the evolution of the crack length according to the number of cycles (Fig. 18). With the high thermal range, the crack propagates more quickly than for low temperature range.

3.3.2. Network crack propagation

This part presents the results of the propagation of a network of 15 cracks. As we specified previously, the spacing between cracks corresponds to the smallest distance observed in experiments. In our case the spacing corresponds to the distance between cracks of eight grains. The evolution of the network (Fig.

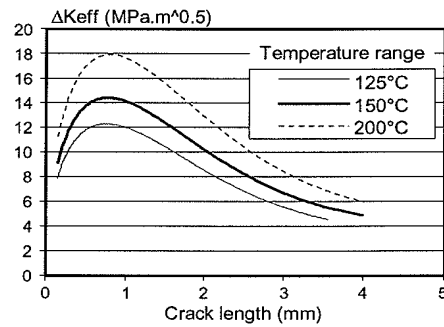


Fig. 17. Effective stress intensity factor versus to crack length in SPLASH test ($T_{\max} = 320\text{ }^{\circ}\text{C}$).

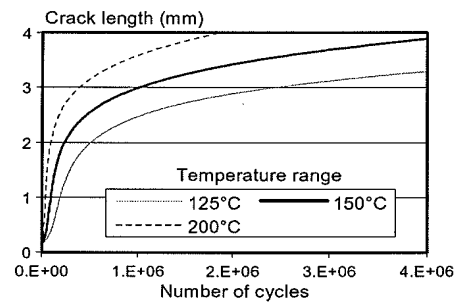


Fig. 18. Simulation of single crack growth in SPLASH test ($T_{\max} = 320\text{ }^{\circ}\text{C}$).

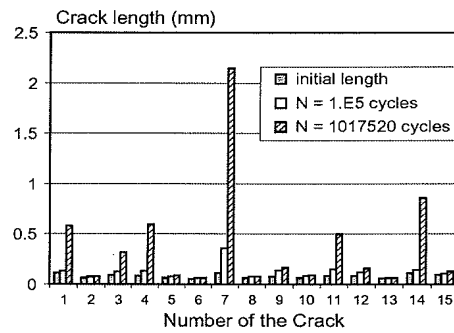


Fig. 19. Crack network propagation ($T_{\max} = 320\text{ }^{\circ}\text{C}$, $\Delta T = 150\text{ }^{\circ}\text{C}$).

19) shows that propagation is favored in the middle of the specimen. At one million cycles, only the central crack is able to propagate until 2.2 mm. This result is in agreement with the experimental results obtained for different temperature ranges (Maillot, 2004). It shows that SPLASH thermal loading is more important

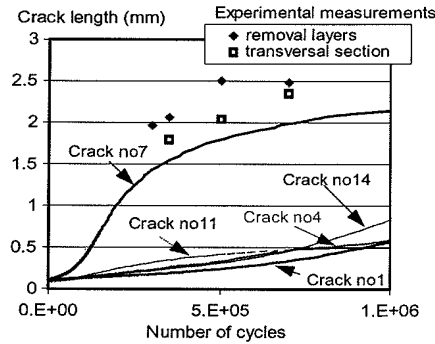


Fig. 20. Crack length versus the number of cycles: comparison with experimental measurements.

than the effect of crack shielding. Nevertheless, the propagation of the crack no. 7 has to contribute to the deceleration of cracks nos. 4 and 11. It should be noted that peripheral cracks (crack nos. 1 and 14) are propagated in spite of a lower load level. Its cracks benefit from the minimal shielding effect.

By comparing the results of the simulations (those of the longest cracks) and the results obtained in experiments (Fig. 20), we notice that the simulation underestimates the maximum crack length. Nevertheless, the tendencies are comparable, with a deceleration of the cracks towards a depth of 2.5 mm. An important result that of the simulation is the behavior of the other cracks and their stability. Indeed, it is noted that the propagation of the central crack inhibits the propagation of cracks nos. 4 and 11, but the peripheral cracks benefit from the absence of any shielding effect to propagate at the end of the test (Fig. 20).

For a more critical temperature range ($\Delta T = 200^\circ\text{C}$) and the same initial configuration of the network, (Fig. 21) we obtain the same results with the kinetics of the propagation more pronounced than for a $\Delta T = 150^\circ\text{C}$.

Fig. 22 shows that a higher temperature range promotes network stabilization assuming always the same configuration: a central crack and two peripherals cracks which start their propagation.

Figs. 23 and 24 show an example of a configuration of the network of cracks obtained by thermal fatigue after 99,000 cycles and 1 million cycles respectively, as well as the meshing of the cracked zone.

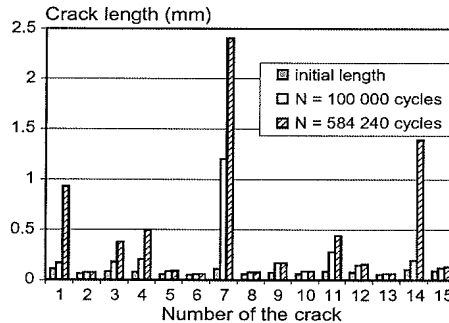


Fig. 21. Crack network propagation ($T_{\text{max}} = 320^\circ\text{C}$, $\Delta T = 200^\circ\text{C}$).

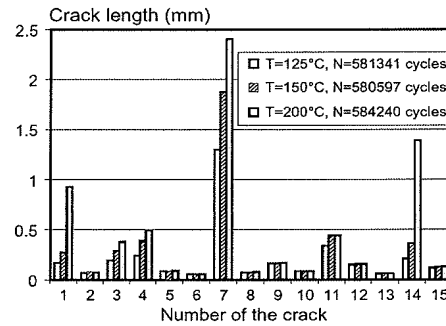
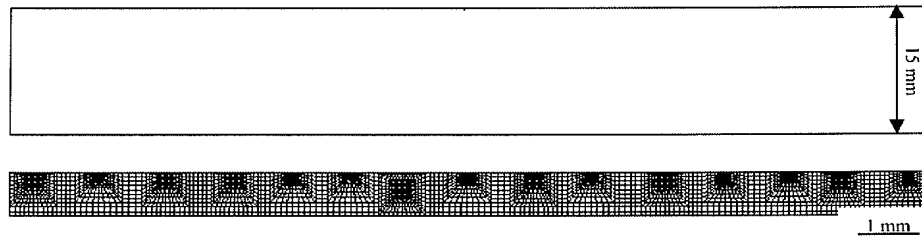
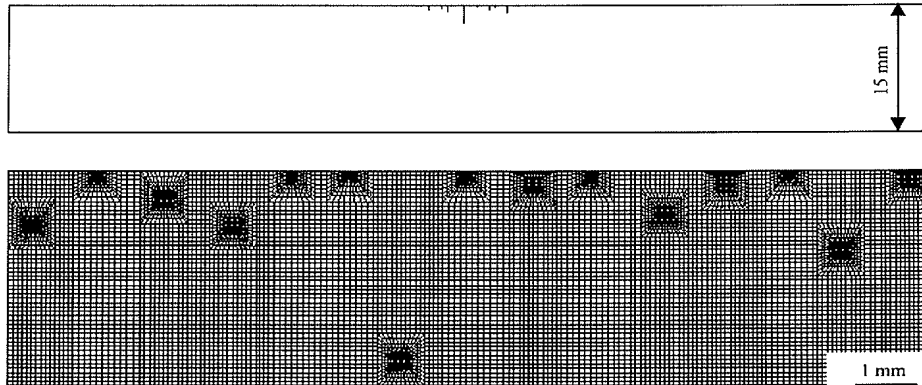


Fig. 22. Temperature effect on the crack network growth.

Fig. 23. Finite element mesh of crack network, $N = 99,000$ cycles ($T_{\max} = 320$ °C, $\Delta T = 150$ °C).Fig. 24. Finite element mesh of crack network $N = 1,057,000$ cycles ($T_{\max} = 320$ °C, $\Delta T = 150$ °C).

3.3.3. Discussion

The results obtained within the framework of this paper are rather encouraging. Indeed, such a simulation, although it is simple, enabled us to reproduce the experimental results in terms of the final configu-

ration of the network and especially in terms of the maximum depth of the cracks. Nevertheless, some points still must be improved, which—in our opinion—are due to some simplifying assumptions:

The first assumption is the simultaneous initiation of all cracks. In experiments, it is observed that stabilization is obtained after 400,000 cycles for ΔT of 150 °C as shown in Fig. 2. Before this stage, we observe a continuing initiation of new cracks on the surface during cycling. Such a deviation of our model assumption from the observed reality could explain the variation obtained between our simulation results and the experimental depths (Fig. 20). Taking into account this phenomenon in a separate simulation appears very important to us, it will therefore be the focus of our next work.

Secondly, we assume that there is no coupling between the cracks and the stress field. It is clear that the presence of cracks in the structure contributes to a relaxation of the stress.

Finally, the last likely point of improvement is the equation governing crack propagation. Actually, we applied Paris' law starting from the initial size of the cracks. But we are quite conscious that the short cracks of such a size propagate with a higher speed than that predicted by Paris' law. In this context, we could take as a starting point the work of Tomkins (1974), Skelton (1988) and Murakami (1988) by expressing the propagation velocity in terms of the loading parameters and as a function of the size of the crack.

4. Conclusions

We construct a crack propagation model that predicts the growth of the crack network under thermal loading. A modified fracture mechanics Paris relation (Skelton method) was used based on an elastic equivalent stress measure. An effective stress intensity factor is calculated taking into account shielding effects.

We have developed a simple and efficient automatic remeshing algorithm. This algorithm, together with the Skelton methodology and a modified Paris relation, has been implemented in an automatic two-dimensional crack propagation program, which enables to simulate the evolution of a crack network.

The present approach is applied to various examples. It is demonstrated that the simulations agree reasonably well with the experimental results obtained for SPLASH conditions. Such a program thus gives an estimation of shielding effects and of the network stability under thermal loading conditions.

References

- Binder, K., Heermann, D.W., 2002. Monte Carlo simulation in statistical physics: An introduction, Fourth ed. Springer, Berlin.
- Bressers, J., Rémy, L., 1996. Fatigue under Thermal and Mechanical Loading. Kluwer Acad. Pub.
- Buchalet, C.B., Bamford, W.H., 1976. Mechanics of crack growth ASTM STP 590, pp. 385–402.
- Chaboche, J.-L., 1989. Constitutive equation for cyclic plasticity and cyclic viscoplasticity. *International Journal of Plasticity* 5 (3), 247–302.
- Cipière, M.F., Le Duff, J.A., 2001. Thermal fatigue experience in French piping. *International Institute of Welding. Document no. XIII-1891-01*, Lubyana.
- Fissolo, A., Marini, B., Nais, G., Wident, P., 1996. Thermal fatigue behaviour for a 316L type steel. *Journal of Nuclear Materials* 233–237, 156–161.
- Fissolo, A., Robertson, C., Maillot, V., Marini, B., 2000. Prediction of cracking under thermal fatigue. In: *Proceedings of ECF 13*, San Sebastian, Spain, 6–9 September 2000.
- Keroulas, F., Thomeret, B., 1990. *Société Française d'Energie Nucléaire*, vol. 1, pp. 107–117.
- Maillot, V., et al., 2004. Thermal fatigue crack networks parameters and stability: an experimental study. *International Journal of Solid and structure*.
- Maillot, V., 2004. Amorçage et propagation de réseaux de fissures de fatigue thermique dans un acier inoxydable austénitique de type x2CrNi 18-09 (AISI 304L). Thesis CEA-R-6041.
- Murakami, Y., 1988. Correlation between strain singularity at crack tip under overall plastic deformation and the exponent of the Coffin–Manson law. In: Salomon, H.D., Halford, G.R. (Eds.), *Low Cycle Fatigue*, ASTM STP 942, pp. 1048–1065.

- Skelton, R.P., 1983. Crack initiation and growth in simple metal components during thermal cycling. *Fatigue at High Temperature*, 1–61.
- Skelton, R.P., 1988. Application of small specimen crack growth data to engineering components at high temperature: a review. In: Salomon, H.D., Halford, G.R. (Eds.), *Low Cycle Fatigue*, ASTM STP 942, pp. 209–235.
- Spera, D.A., Mowbray, D.F., 1976. Thermal fatigue of materials and components. *ASTM STP 612*.
- Tomkins, B., 1974. Fatigue crack propagation—an analysis. *Philosophical Magazine* 18, 1041–1066.

Exhibit B

Ads by Google

Stainless Steel

Thermal Expansion

Linear Expansion

Copper Metals

Steel Metals



The Engineering ToolBox

www.EngineeringToolBox.com

Resources, Tools and Basic Information for Engineering and Design of Technical Applications!

Search

 Google™
Custom Search

Coefficients of Linear Expansion

Linear temperature expansion coefficients for some common materials as aluminum, copper, glass, iron and many more

Sponsored Links

Thermal Expansion Maintain fits between round parts like bearings and gears usatolerancings.com

Bellows Expansion Joints Metal Bellows Expansion Joints in Every Style from Flexicraft www.Flexicraft.com/Metal_Bellows

Ads by Google

Thermal expansion coefficients for some common materials can be found in the table below:

Product	Linear Temperature Expansion Coefficient - α -	
	(10 ⁻⁶ m/m K)	(10 ⁻⁶ in/in °F)
ABS (Acrylonitrile butadiene styrene) thermoplastic	73.8	41
ABS -glass fiber-reinforced	30.4	17
Acetal	106.5	59.2
Acetal - glass fiber-reinforced	39.4	22
Acrylic, sheet, cast	81	45
Acrylic, extruded	234	130
Alumina	5.4	3.0
Aluminum	22.2	12.3
Antimony	10.4	5.8
Arsenic	4.7	2.6
Barium	20.6	11.4
Beryllium	11.5	6.4
Bismuth	13	7.3
Brass	18.7	10.4
Brick masonry	5.5	3.1
Bronze	18.0	10.0
Cadmium	30	16.8
Calcium	22.3	12.4
Carbon - diamond	1.2	0.67
Cast Iron Gray	10.8	6.0
Cellulose acetate (CA)	130	72.2
Cellulose acetate butynate (CAB)		80 - 95
Cellulose nitrate (CN)	100	55.6
Cement	10.0	6.0
Cerium	5.2	2.9
Chlorinated polyvinylchloride (CPVC)	66.6	37
Chromium	6.2	3.4
Clay tile structure	5.9	3.3
Cobalt	12	6.7
Concrete	14.5	8.0
Concrete structure	9.8	5.5
Constantan	18.8	10.4
Copper	16.6	9.3
Copper, Beryllium 25	17.8	9.9
Corundum, sintered	6.5	3.6
Cupronickel 30%	16.2	9
Diamond	1.1	0.6
Dysprosium	9.9	5.5
Ebonite	76.6	42.8

Epoxy, castings resins & compounds, unfilled	55	31
Erbium	12.2	6.8
Ethylene ethyl acrylate (EEA)	205	113.9
Ethylene vinyl acetate (EVA)	180	100
Europium	35	19.4
Fluoroethylene propylene (FEP)	135	75
Gadolinium	9	5
Germanium	6.1	3.4
Glass, hard	5.9	3.3
Glass, Pyrex	4.0	2.2
Glass, plate	9.0	5.0
Gold	14.2	8.2
Granite	7.9	4.4
Graphite, pure	7.9	4.4
Hafnium	5.9	3.3
Hard alloy K20	6	3.3
Hastelloy C	11.3	6.3
Holmium	11.2	6.2
Ice	51	28.3
Inconel	12.6	7.0
Indium	33	18.3
Invar	1.5	0.8
Iridium	6.4	3.6
Iron, pure	12.0	6.7
Iron, cast	10.4	5.9
Iron, forged	11.3	6.3
Lanthanum	12.1	6.7
Lead	28.0	15.1
Limestone	8	4.4
Lithium	46	25.6
Lutetium	9.9	5.5
Magnesium	25	14
Manganese	22	12.3
Marble	5.5 - 14.1	3.1 - 7.9
Masonry	4.7 - 9.0	2.6 - 5.0
Mica	3	1.7
Molybdenum	5	2.8
Monel	13.5	7.5
Mortar	7.3 - 13.5	4.1-7.5
Neodymium	9.6	5.3
Nickel	13.0	7.2
Niobium (Columbium)	7	3.9
Nylon, general purpose	72	40
Nylon, Type 11, molding and extruding compound	100	55.6
Nylon, Type 12, molding and extruding compound	80.5	44.7
Nylon, Type 6, cast	85	47.2
Nylon, Type 6/6, molding compound	80	44.4
Osmium	5	2.8
Palladium	11.8	6.6
Phenolic resin without fillers	80	44.4
Plaster	16.4	9.2
Platinum	9.0	5.0
Plutonium	54	30.2
Polyallomer	91.5	50.8
Polyamide (PA)	110	61.1
Polybutylene (PB)		72
Polycarbonate (PC)	70.2	39
Polycarbonate - glass fiber-reinforced	21.5	12
Polyester	123.5	69

Polyester - glass fiber-reinforced	25	14
Polyethylene (PE)	200	111
Polyethylene (PE) - High Molecular Weight		60
Polyethylene terephthalate (PET)	59.4	33
Polyphenylene - glass fiber-reinforced	35.8	20
Polypropylene (PP), unfilled	90.5	50.3
Polypropylene - glass fiber-reinforced	32	18
Polystyrene (PS)	70	38.9
Polysulfone (PSO)	55.8	31
Polyurethane (PUR), rigid	57.6	32
Porcelain	3.6	2.0
Potassium	83	46.4
Polyvinyl chloride (PVC)	50.4	28
Polyvinylidene fluoride (PVDF)	127.8	71
Porcelain	4.5	2.5
Potassium	83	46.1
Praseodymium	6.7	3.7
Promethium	11	6.1
Quartz	0.77 - 1.4	0.43 - 0.79
Rhenium	6.7	3.7
Rhodium	8	4.5
Rubber, hard	77	42.8
Ruthenium	9.1	5.1
Samarium	12.7	7.1
Sandstone	11.6	6.5
Scandium	10.2	5.7
Selenium	3.8	2.1
Silicon	5.1	2.8
Silver	19.5	10.7
Slate	10.4	5.8
Sodium	70	39.1
Solder 50 - 50	24.0	13.4
Steatite	8.5	4.7
Steel	13.0	7.3
Steel Stainless Austenitic (304)	17.3	9.6
Steel Stainless Austenitic (310)	14.4	8.0
Steel Stainless Austenitic (316)	16.0	8.9
Steel Stainless Ferritic (410)	9.9	5.5
Strontium	22.5	12.5
Tantalum	6.5	3.6
Tellurium	36.9	20.5
Terbium	10.3	5.7
Terne	11.6	6.5
Thallium	29.9	16.6
Thorium	12	6.7
Thulium	13.3	7.4
Tin	23.4	13.0
Titanium	8.6	4.8
Tungsten	4.3	2.4
Uranium	13.9	7.7
Vanadium	8	4.5
Vinyl Ester	16 - 22	8.7 - 12
Wood, fir	3.7	2.1
Wood, oak parallel to grain	4.9	2.7
Wood, oak across to grain	5.4	3.0
Wood, pine	5	2.8



ime
coustics
Psychrometrics
asics
ombustion
ynamics
conomics
lectrical
nvironment
uid Mechanics
as and Compressed
ir
IVAC Systems
draulics and
neumatics
sulation
aterial Properties
athematics
technics
iscellaneous
hysiology
iping Systems
rocess Control
umps
standards
rganizations
team and
ondensate
hermodynamics
ater Systems

Ads by Google
Aluminum Steel
Aluminum Metals
Copper Aluminum
Aluminum Volume
Copper Steel

ToolBox ShortList
• Add this Page!

Google™

Search the ToolBox!

Translate this
Page!!

About Us!

Temperature

0

☒ °C
☐ °F

Convert!

Length

1

☒ m
☐ km
☐ in
☐ ft
☐ yards
☐ miles
☐ nautical
miles

Convert!

Volume

1

Ytterbium	26.3	14.6
Yttrium	10.6	5.9
Zinc	29.7	16.5
Zirconium	5.7	3.2

- $T(^{\circ}C) = 5/9[T(^{\circ}F) - 32]$
- 1 in (inch) = 25.4 mm
- 1 ft (foot) = 0.3048 m

- [Calculate Thermal Pipe Expansion](#)

Custom & STD Flanges Large Diameter, Slip-Ons, Weld Neck Blind, Custom Flanges, any material [coastalflange.com](#)

Protective Paints Corrosion Resistant Coatings Liquid (Solvent or Water) Powder [www.atomizedmaterials.com](#)

Integrated Rail Systems Maytec Style Frame+Embedded Raceway Flexible, Smooth & Accurate Travel [www.PBClinea](#)

Ads by Google

Related Topics

- [Material Properties](#) - Material properties - density, heat capacity, viscosity and more - for gases, fluids and solids
- [Temperature Expansion](#) - Thermal expansion of pipes and tubes - stainless steel, carbon steel, copper, plastics and more
- [Thermodynamics](#) - The effects of work, heat and energy on a system

Sponsored Links

Stainless Steel Filter Screens Welded, Woven, & Filter Mesh Wire Pick The Metal & Style For Your Use [www.DirectMe](#)

Thomson Linear Guides Quality Linear Guide Systems From Thomson. Get Free Resources Now, [ThomsonLinear.com/L](#)

Low Cost Linear Solution Alternative aluminum frame profile rails embedded with steel raceways [www.PBClinea.com](#)

Ads by Google

Related Documents

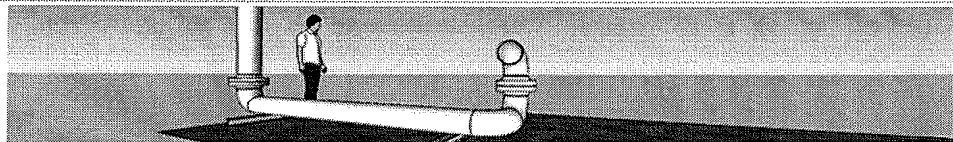
- [Assembly of Shrink-Fits](#) - Heating temperature of shrink-fits
- [Change in Radius of Thin Circular Ring with Temperature](#) - Change in pipe diameter with temperature change
- [Expansion Loop Capacities - Copper Tubes](#) - Capacity of expansion loops - copper tubes
- [Expansion of Copper, Carbon and Stainless Steel Pipes](#) - Thermal expansion of stainless steel, carbon steel pipes and copper tubes
- [PVC Pipes - Expansion Loops](#) - Temperature expansion and contraction in PVC piping systems
- [Pipes and Tubes - Temperature Expansion](#) - Pipes expands when heated and contracts when cooled. The expansion of the pipes can be expressed with the expansion formula
- [Pressfit Pipes Expansion Loops](#) - Pressfit pipes and design of temperature expansion loops
- [Steel Pipes and Temperature Expansion](#) - Temperature expansion of carbon steel pipes
- [Temperature Expansion Coefficients of some common Piping Materials](#) - Expansion coefficients of some common materials used for pipes and tubes - aluminum, carbon steel, cast iron, PVC, HDPE and more
- [Temperature Expansion of Steam Pipes](#) - Thermal heating and cooling expansion of pipes in cast iron, carbon and carbon molybdenum steel, wrought iron, copper, brass and aluminum
- [Thermal Expansion - Linear](#) - Linear temperature expansion - online calculator
- [Thermal Expansion Metals](#) - Thermal expansion of some common metals

ToolBox Short List

Difficult to find your favorite ToolBox page? Add links to your favorite pages in your own personal Short List!

• [Add this Page!](#) • [Delete the ShortList!](#)

Engineering ToolBox - SketchUp Edition - Online 3D modeling!



[Engineering ToolBox - SketchUp Edition](#) - enabled for use with the amazing, fun and free [Google SketchUp](#).

Search the ToolBox

Search

Translate the ToolBox

Engineering News



PrinterFriendly

ToolBox ShortList
• [Add this Page!](#)

[Link to this Page!](#)

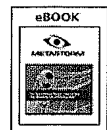
[BookMarkThe
Engineering ToolBox!](#)

Sponsored Links [BookMark this Page!](#)

ADD THIS

Free Industry
Resources

The Best Process
Wins® - How to
Run Your Business
like a Winning
Team



How Do You Know
if Your Talent
Management
Strategy is Creating
Value?



VDI Expert Series -
XenDesktop: The
Next Generation of
Desktop
Virtualization



Industry standards
online:
ASM, ASME, IEEE,
ISO, API